Heliyon 10 (2024) e39185

Contents lists available at ScienceDirect

Heliyon

journal homepage: www.cell.com/heliyon

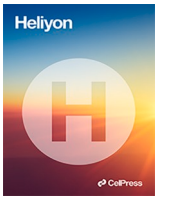

Research article

3D microstructure reconstruction and characterization of porous materials using a cross-sectional SEM image and deep learning

Xianhang Li [a], Shihao Zhou [a], Xuhao Liu [a], Jiadong Zang [b], Wenhao Fu [b], Wenlong Lu [b], Haibo Zhang [c,**], Zilin Yan [a,*]

[a] School of Science, Harbin Institute of Technology, Shenzhen, 518055, China
[b] Shenzhen Geekvape Technology Co., Ltd, Shenzhen, 518102, China
[c] School of Materials Science and Engineering, State Key Laboratory of Material Processing, Die & Mould Technology, Huazhong University of Science and Technology, Wuhan, 430074, China

ARTICLE INFO

Keywords:
Porous media
3D reconstruction
Microstructure characterization
Generative adversarial networks
Deep learning

ABSTRACT

Accurate assessment of the three-dimensional (3D) pore characteristics within porous materials and devices holds significant importance. Compared to high-cost experimental approaches, this study introduces an alternative method: utilizing a generative adversarial network (GAN) to reconstruct a 3D pore microstructure. Unlike some existing GAN models that require 3D images as training data, the proposed model only requires a single cross-sectional image for 3D reconstruction. Using porous ceramic electrode materials as a case study, a comparison between the GAN-generated microstructures and those reconstructed through focused ion beam-scanning electron microscopy (FIB-SEM) reveals promising consistency. The GAN-based reconstruction technique demonstrates its effectiveness by successfully characterizing pore attributes in porous ceramics, with measurements of porosity, pore size, and tortuosity factor exhibiting notable agreement with the results obtained from mercury intrusion porosimetry.

1. Introduction

Porous materials can be found in nature or can be synthesized for specific needs. Porous materials possess various applications due to their distinctive properties like high surface area, selective permeability, and customizable pore characteristics. They find uses in fields such as electrochemical devices [1,2], catalysis [3,4], gas storage [5–7], purification and filtration [8–10], drug delivery [11,12], thermal insulation [13–15], biomedical implants [16], energy storage [17], and more. They are crucial for addressing challenges related to environmental sustainability, energy efficiency, and advanced technology development. It is well established that the functionalities of porous materials and the performance of porous devices can be engineered and customized by manipulating porosity [18], pore size [19], and pore orientation [20] within the materials.

Accessing the pore characteristics is of great interest for understanding, predicting, and boosting the performance and durability of porous materials and devices. Depending on the accuracy and pore size range to measure, there are a number of measures to characterize the pore characteristics of porous materials. The gas adsorption method, also known as the Brunauer-Emmett-Teller (BET) method [21], is widely used to determine specific surface area, pore volume, and pore size distribution of porous media. Mercury

* Corresponding author.
** Corresponding author.
E-mail addresses: hbzhang@hust.edu.cn (H. Zhang), yanzilin@hit.edu.cn (Z. Yan).

https://doi.org/10.1016/j.heliyon.2024.e39185
Received 29 April 2024; Received in revised form 8 October 2024; Accepted 9 October 2024
Available online 10 October 2024

intrusion porosimetry (MIP) [22] involves immersing a sample in mercury and measuring the amount of mercury intruded into the pores as pressure increases. It provides information about pore size distribution and total pore volume; the pore size that can be measured usually ranges from a few nanometers to thousands of microns. Optical microscopy (OM) and scanning electron microscopy (SEM) [23] provide morphological images of the cross-sectional or surface microstructures of porous materials and can give qualitative information about pore size, pore size distribution, and pore morphology. However, the 2D pore information does not accurately reflect the 3D spatial percolation of the pores and potential anisotropy of the pores. X-ray computed tomography (X-ray CT) [24,25] is widely used to visualize the internal microstructure of porous materials. It provides detailed 3D images that reveal pore sizes, shapes, and connectivity. X-ray CT can also be combined with other techniques, like image segmentation and analysis software, to quantify pore characteristics. Focused ion beam-scanning electron microscopy (FIB-SEM) tomography [26,27], is an alternative 3D reconstruction technique used to visualize and analyze the 3D microstructure of materials at the nanoscale. 3D images provide a comprehensive view of the internal microstructure of the material, allowing accurate characterization of pore size, shape, distribution, and connectivity. 3D images enable more accurate and reliable quantitative analysis of pore parameters, leading to a better understanding of the material's properties. Combined with 3D microstructures, numerical methods such as computational fluid dynamics (CFD) [28,29] and lattice Boltzmann method (LBM) [30,31] can be used to simulate the mass and heat transfer and electrochemical reactions in porous materials such as the porous electrodes in fuel cells. Liu et al. [32] utilized finite element method (FEM) to predict mechanical properties of porous ceramics based on their 3D microstructures. Zhang et al. [33] investigated the permeability of C/SiC porous ceramics using simulations based on 3D microstructures obtained via X-ray CT. However, acquiring 3D images often requires more time and specialized equipment, such as an X-ray transmission microscope (with an X-ray irradiation source) or a FIB-SEM system, making it less suitable for rapid analysis.

Alternatively, some algorithms have been developed to reconstruct the 3D pore information from 2D porous microstructures. Stochastic reconstruction of porous materials is a computational technique used to generate realistic 3D representations of porous structures based on statistical information obtained from experimental data or theoretical models using a simulated annealing algorithm [34]. This approach involves numerically synthesizing porous materials with similar statistical properties to the real materials of interest. Stochastic reconstruction is particularly valuable when there is limited access to tomography facilities. Although the stochastic reconstruction method can be applied to reconstruct various types of porous media, its low efficiency and massive calculation limit its application.

With the advent of machine learning and deep learning, the reconstruction of 3D porous materials using deep learning techniques like generative adversarial networks (GANs) is an exciting area of research that leverages deep learning to generate realistic and complex porous structures. Mosser et al. [35] firstly introduced a GAN-based approach to generate 3D porous media which relies on 3D images as training dataset. Ma et al. [36] built a conditional GAN to reconstruct the 3D image of Berea sandstone porous material. With the porosity as a controlling condition, porous microstructure with different porosities and more diversities can be generated for further analysis. Similarly, Kishimoto et al. [37] utilized a conditional GAN to reconstruct 3D microstructure of porous composite anode materials of solid oxide fuel cells (SOFCs) with controlled volume fraction of different phases. Shams et al. [38] coupled a GAN and an auto-encoder (AE) neural network to reconstruct 3D multi-scale porous media enabling reconstruction of the inter-grain and intra-grain pore space. In this model, the input dataset also requires 3D images. Later on, Shams et al. [39] proposed a novel statistical and conditional GAN (ST-GAN) to reconstruct 3D porous microstructure from 2D cross-section. The coupled method can efficiently reconstruct heterogeneous porous media with pre-processed statistical metrics as constraints. The model training necessitates a large computational effort and network adjustment. Zhang et al. [40] firstly proposed a recurrent neural network (RNN)-based model, 3D-PMRNN, for 3D reconstruction of a porous structure layer-by-layer. In this model, the morphological features of a 2D image were learned by the CNN, while the spatial correlation between adjacent layers was learned by the RNN. Once the model was trained, the reference image was input into the model, and sequential images could be generated to reconstruct a 3D image. However, this method will lose accuracy when the 3D microstructure is anisotropic along the *Z* direction. This model was later improved by integrating a GAN with the RNN-based model to improve the randomness and diversity along the *Z* direction. Zheng et al. [41] proposed a new framework combining VQ-VAE and conditional GPT, to synthesize 3D microstructure based on a single 2D slice. In this model, the VQ-VAE was utilized to compress the sequence of continuous rock slices to discrete latent vectors. Then a conditional GPT was employed to model these discrete latent vectors in an autoregressive manner while incorporating conditional information, such as given 2D slices, rock type and porosity. Once the model was trained, it could produce multiple kinds of rocks simultaneously that also satisfy user-defined properties. For these 2D-to-3D reconstruction models, continuous 2D slices of at least of one 3D microstructure of the sample was required for training although a single 2D image was enough for 3D image synthesis. In practice, acquisition of 3D microstructures is inconvenient or expensive. Thus, training a 2D-to-3D model which only requires cross-section images seems to be of cost-effectively significant.

In this context, this study proposes a GAN framework to reconstruct a 3D pore microstructure from a single 2D microstructure of the porous material, building on Ketch and Cooper's original SliceGAN [42], without the need for 3D images as training data. We conduct a comparative analysis between the microstructures reconstructed via GAN and those true microstructures achieved through FIB reconstruction, thereby assessing the GAN-generated microstructures in terms of specific surface area, porosity, and tortuosity factors. Moreover, the proposed approach is subject to validation by predicting the diverse pore characteristics within additional porous ceramic samples. These predictions are then compared with outcomes obtained from mercury intrusion porosimetry experiments on the same set of porous ceramic samples.

2. Experimental and methods

2.1. FIB-SEM 3D reconstruction of porous ceramic materials

Two porous ceramic electrode materials for SOFCs (SOFC #1 and #2) were selected for the case study. The two samples were impregnated with epoxy resin under vacuum for 24 h until the epoxy resin was fully cured. The samples were removed and ground with sandpaper to expose the samples' cross-section, and the cross-section was finely polished using an argon-ion beam cross-section polisher (CP). A scheme using spherical particles as references to correct reconstruction distortion with the FIB-SEM reconstruction technique was adopted in this study. Detailed sample preparation can be found in a previous publication [43]. The schematic of the FIB-SEM is shown in Fig. 1. A dual-beam focused ion beam-scanning electron microscope (Crossbeam 540, Zeiss) used in this experiment, with a lateral resolution of 24 nm (*x, y* direction) and a slice pitch of 24 nm (*z*-direction), was operated automatically for 8 h to obtain a continuous sequence of 2D images. According to an established image processing procedure involving alignment, de-shading, filtering, and cropping in a previous publication [44] and correction with de-shearing treatment, we obtained the 3D microstructures of the SOFC samples. As can be seen, there is no "pore back" effect and the pores are all black in the image, which benefits from the resin impregnation under vacuum.

2.2. 2D microstructure acquisition with SEM

The resolution of the nowadays SEM can reach as high as a few nanometers which enables the capturing of the nanosized features of the porous materials. However, for some porous materials, the pore features are quite diverse and the pore size ranges from a few nanometers to hundreds of microns. In this case, the reconstructed volume by the FIB-SEM reconstruction will be too limited to be representative of the entire microstructure as the nanometric features have to be captured with high magnifications. Although large pores can be captured at low magnifications, FIB milling of large volumes can be another challenge for the FIB-SEM reconstruction technique. By referring to the previous section, the same process of vacuum impregnation, grinding, and CP polishing was carried out on two additional porous ceramics atomizer core samples provided by *Shenzhen Geekvape Technology Co., Ltd*, and cross-sections of these two samples were obtained. Then, a backscattering electron (BSE) detector was used to obtain a 2D image of the cross-section of the samples. In order to capture the large pores (hundreds of microns), the resolution of the SEM was set to 3.35 μm per pixel. That means the features of the particles or the pores beyond this resolution were not captured on the images. Fig. 2 shows the original grayscale SEM images of the samples GV #1 (Fig. 2 (a)) and GV #2 (Fig. 2 (c)). It is seen that sharp contrast between the solid and pores (filled by resin) can be achieved thanks to the resin impregnation treatment. By using the thresholding plugin in ImageJ, the solid and pore phases can be segmented and the corresponding binarized images of samples GV #1 and GV #2 are shown in Fig. 2 (b) and (d), respectively. The thresholding value was fine-tuned to ensure that the porosity measured from binarized images matches the porosity by mercury intrusion porosimetry method (detailed in Section 3.5). It is seen that there are more fine pores in sample GV #1 than in sample GV #2. The largest pores in the two samples are estimated to be a few hundred microns.

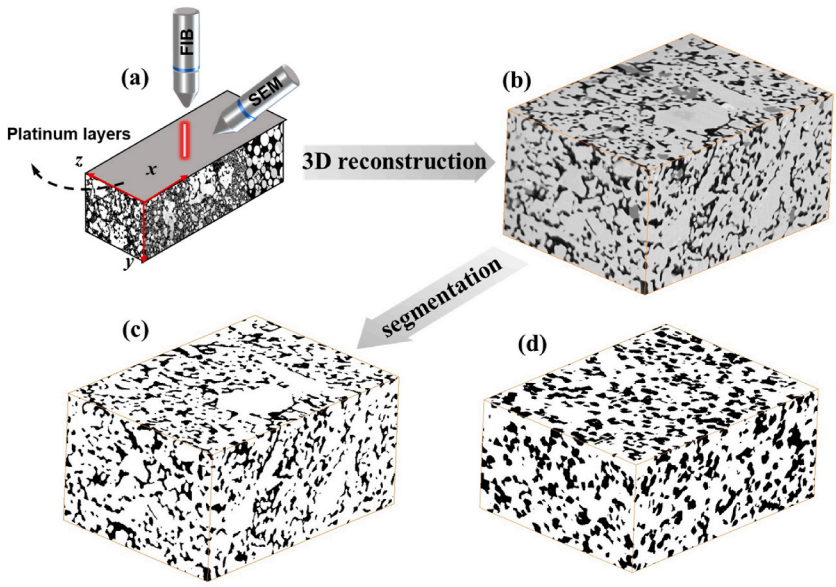

Fig. 1. FIB-SEM 3D reconstruction of the porous ceramics: (a) Schematic of the dual beam FIB-SEM reconstruction; (b) Reconstructed 3D microstructure based on the sequence of original grayscale images; (c) Binarized 3D microstructures of sample SOFC #1; and (d) sample SOFC #2 with the white phase as the solids and black phase as the pores.

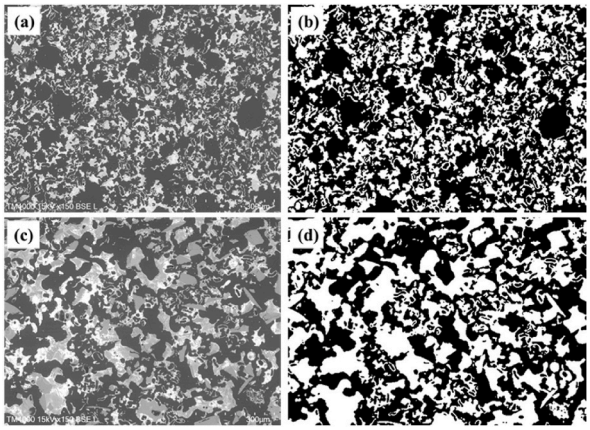

Fig. 2. SEM images of the porous ceramic atomizer core samples provided by *Geekvape Technology*: (a) and (b) are grayscale and binarized SEM images of sample GV #1; (*c*) and (*d*) are grayscale and binarized SEM images of sample GV #2.

2.3. 3D reconstruction with generative adversarial network (GAN)

The principle of GANs involves the interaction of two neural networks, *i.e.*, a generator network and a discriminator network, in a competitive learning framework. The generator aims to create data that is indistinguishable from real data, while the discriminator's role is to differentiate between real data and data generated by the generator. As the training proceeds, GANs improve the generator's ability to produce increasingly realistic output by minimizing the discriminator's ability to differentiate. This adversarial process results in the generator producing highly convincing data, making GANs a powerful tool for tasks like image synthesis data augmentation, and 3D reconstruction of objects [45,46]. A traditional GAN follows a min-max game with a loss function that is formally defined as:

$$\min_{G}\max_{D}\left\{E_{x\sim p_{data}}[\log D(x)]+E_{z\sim p_{noise}}[\log(1-D(G(z)))]\right\}, \tag{2}$$

where x is a real instance input in discriminator D, p_{data} is the data distribution of the training dataset, $\boldsymbol{z}$ is a latent vector randomly sampled from noise distribution dataset p_{noise}, $D(x)$ is the output scalar of D which stands for the possibility of x being sampled from the training dataset. And G is trained to build a functional relationship between $\boldsymbol{z}$ and data space $G(\boldsymbol{z})$, by minimizing the probability that D distinguishes $G(\boldsymbol{z})$ came from p_{noise} rather than p_{data}. In the original GAN method, the Kullback–Leibler divergence is minimized when

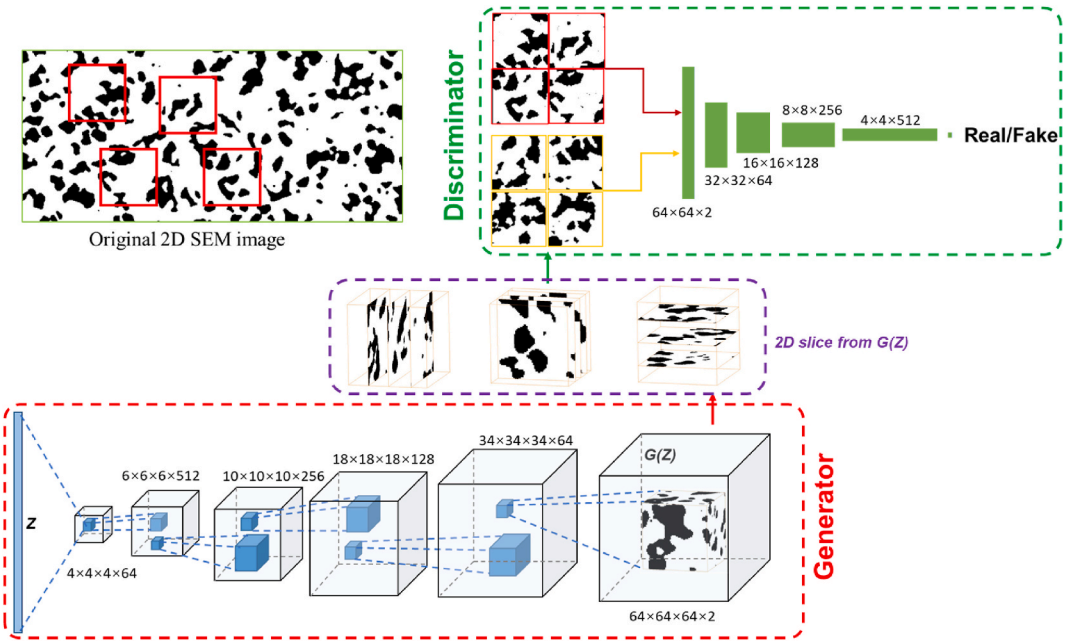

Fig. 3. The GAN architecture adopted in this study.

training the networks to generate fake data. Training deep networks with the gradient descent method tends to lead to unstable learning. A recent study introduced a 3D improved Wasserstein GAN (3D-IWGAN) [47] to fix this drawback by minimizing the Wasserstein distance between the data and generated distributions as below:

$$L = E_{\tilde{x}\sim p_g}[D(\tilde{x})] - E_{x\sim p_r}[D(x)] + \lambda E_{\hat{x}\sim p_{\hat{x}}}\left[\left(\|\nabla_{\hat{x}} D(\hat{x})\|_2 - 1\right)^2\right], \tag{3}$$

where λ is the gradient penalty, p_g and p_r are the generator and target distribution, and $p_{\hat{x}}$ is the distribution sampling uniformly on a straight line between p_g and p_r.

In this study, we adopted a similar 3D-IWGAN deep learning algorithm for the 3D reconstruction of isotropic microstructure from a single 2D microstructure. The architecture of the 3D-IWGAN adopted in the current study is shown in Fig. 3. As shown in Fig. 3, in the generator network, a latent vector $\boldsymbol{z}$ (noise) is the only input parameter, and then multiple 3D transpose convolutions are performed to unfold the one-dimension $\boldsymbol{z}$ vector to $64 \times 64 \times 64 \times 2$ output tensor, which can be expressed as $G(\boldsymbol{z})$. The output corresponds to a 3D microstructural image of a two-phase material. The 3D image generated from $G(\boldsymbol{z})$ is sliced along three directions x, y, and z at one voxel increment. In the discriminator, 2D real and fake images are as input data. For each fake 2D image input, a real 2D image is randomly cut from the original 2D SEM image. The current model is similar to the SliceGAN model described in *Ref.* [48]. The reconstruction algorithm is demonstrated by the following pseudocode.

Algorithm 1. The 2D-to-3D GAN for 3D Microstructure Reconstruction

Require: The gradient penalty coefficient λ, the number of D iterations per G iteration n_D, the batch sizes m_D and m_G for D and G, respectively, Adam hyperparameters α, β_1, β_2.
Require: initial critic parameters w_0, initial generator parameters θ_0.
1: while θ has not converged do
2: Generator training:
3: for t = 1, …, n_D do
4: for i = 1, …, m_D do
5: Sample a latent vector from a normal distribution $\boldsymbol{z} \sim \boldsymbol{p}(\mathbf{z})$
6: $\tilde{\boldsymbol{x}} \leftarrow G_0(\mathbf{z})$ generate a 3D volume
7: for a = 1, 2, 3 do
8: for d = 1, …, l do
9: $\tilde{\boldsymbol{x}}_{2d} \leftarrow$2D slice of $\tilde{x}$ at depth d along axis a
10: Sample an l × l image from the real dataset $\mathbf{x} \sim \boldsymbol{p_r}$
111: Sample a random number $\epsilon \sim U$ [0, 1]
12: $\hat{\boldsymbol{x}} \leftarrow \epsilon\, \mathbf{x} + (1-\epsilon)\, \tilde{\boldsymbol{x}}$
13: $L_D \leftarrow \mathrm{D_w}(\tilde{\boldsymbol{x}}_{2d}) - D_w(\mathbf{x}) + \lambda(||\, \nabla_{\hat{x}}\, \mathrm{D_w}(\hat{\boldsymbol{x}})||_2 - 1)^2$
14: end for
15: end for
16: $\mathrm{w} \leftarrow \mathrm{Adam}\left(\nabla_w \frac{1}{m_D} \sum_{a=1}^{3} \sum_{d=1}^{l} L_D\right)$
17: end for 18: Generator training:
19: for j = 1, …, m_G do
20: Sample a latent vector from a normal distribution $\boldsymbol{z} \sim \boldsymbol{p}(\mathbf{z})$
21: $\tilde{\boldsymbol{x}} \leftarrow G_0(\mathbf{z})$ generate a 3D volume
22: for a = 1, 2, 3 do
23: for d = 1, …, l do
24: $\tilde{\boldsymbol{x}}_{2d} \leftarrow$ 2D slice of $\tilde{\boldsymbol{x}}$ at depth d along axis a
25: $L_G \leftarrow -D_w\,(\tilde{\boldsymbol{x}}_{2d})$
26: end for
27: end for
29: end for
28: $\theta \leftarrow \mathrm{Adam}\left(\nabla_\theta \frac{1}{m_G} \sum_{a=1}^{3} \sum_{d=1}^{l} L_G\right)$
30: end while

Table 1
The architecture of the 3D generator.

Layer	Kernel size	Stride	Padding	Output shape
$\boldsymbol{z}$	4	2	2	$4 \times 4 \times 4 \times 64$
1	4	2	2	$6 \times 6 \times 6 \times 512$
2	4	2	2	$10 \times 10 \times 10 \times 256$
3	4	2	2	$18 \times 18 \times 18 \times 128$
4	4	2	2	$34 \times 34 \times 34 \times 64$
5	4	2	3	$64 \times 64 \times 64 \times 2$
Softmax	–	–	–	$64 \times 64 \times 64 \times 2$

The GAN used in this study is composed of a 6-layer generator and a 7-layer discriminator. The hyperparameters for the generator and discriminator are listed in Tables 1 and 2, respectively. A batch size of 8 is adopted for both the generator and discriminator. The Adam optimizer [49] was used, and the Adam optimizer parameters are: $\alpha = 0.0001$, $\beta_1 = 0.9$, $\beta_2 = 0.999$. The gradient penalty coefficient is set to $\lambda = 10$. The learning rates for both the generator and discriminator training were tuned within the range of 10^{-6} to 10^{-3} to achieve a balance between accuracy and time efficiency. Ultimately, the learning rates for the generator and discriminator were both set to 10^{-4}. In this study, using the optimized neural network architecture detailed in Tables 1 and 2, the training process took approximately 30 min on two NVIDIA GeForce RTX 3090 GPUs. Once the model was trained, it took only a few seconds to reconstruct a 3D image with dimensions up to 128 × 128 × 128 voxels.

2.4. Pore analysis based on images

To quantify the pore microstructures, a few important microstructural metrics, such as volumetric (areal) fraction of phases, specific surface area, pore size, pore size distribution, and tortuosity factor are calculated. These metrics are compared for the FIB reconstructed and the GAN reconstructed 3D microcultures of the same samples to evaluate the reliability of the GAN-based 3D reconstruction.

2.4.1. Volumetric/areal fraction

Volumetric fraction (3D) or areal fraction (2D) of the solid or pore phase is defined as the ratio of the total voxels (3D) or pixels (2D) of the phase of interest to the total voxels or pixels of the entire image which represents the microstructure.

2.4.2. Specific surface area

The volume-specific surface area is also known as the surface-area-to-volume ratio, defined as $S_a = S/V$ ($\mu m^2\ \mu m^{-3}$), where S is the total surface area of solids, and V is the total volume of both solid and pore phases. In the present study, the surface area S was calculated using a marching cube method [50]. This advanced algorithm allows the surface curvatures to be considered even if the microstructures are represented in voxels.

2.4.3. Pore size analysis

An image-based SNOW algorithm was used to separate the 3D pore networks into individual pore regions such that each pore can be analyzed. The SNOW algorithm [51] uses a marker-based watershed segmentation algorithm to partition an image into regions belonging to each phase. The main contribution of the SNOW algorithm is to find a suitable set of initial markers in the image so that the watershed is not over-segmented. Suitable initial markers can be controlled by varying the marker size and Gaussian filter parameters: r and sigma values. Fig. 4 shows the pore segmentation of 2D porous microstructure as a demonstration using the SNOW algorithm. Fig. 4(a) and (b) display samples SOFC #1 and SOFC #2, respectively, while Fig. 4 (c) and (d) depict samples GV #1 and GV #2. Note that the SNOW algorithm applies to both 2D and 3D images.

After pore segmentation, the pore size and pore size distribution can be calculated based on all segmented pores. The pore size of each separated porous region is measured using the volume equivalent diameter. The Pore Network Model [52] (PNM) is used to visualize the pore network which is imposed onto the original image as shown in Fig. 5. It is seen that for the samples SOFC #1 (Fig. 5 (a)) and #2 (Fig. 5(b)), the porosities are low, and the pores are just locally connected but disconnected globally. For samples GV #1 (Fig. 5(c)) and #2 (Fig. 5(d)), the porosities are relatively high, and the pores are fully percolated from one side to the opposite side. Fig. 6 shows the FIB-SEM reconstructed 3D microstructures and the PNM within the 3D microstructures of samples SOFC #1 and #2. It shows that the pore networks in the samples SOFC #1 and #2 are actually well connected in the 3D space although the pores are not percolated in the 2D microstructures.

2.4.4. Tortuosity factor

For the 3D microstructure, the tortuosity factor reflects the resistance of the transport of the specific species in a specific phase. For example, the electrical conductivity in the conducting solid phase is correlated to the tortuosity factor of the conducting solid phase in an SOFC electrode; and the gas diffusivity in the pore phase is correlated to the tortuosity factor of the pores in the SOFC electrode. The tortuosity factor can be calculated by a random walker method [43] or Lattice Boltzmann simulations [53]. In this study, the tortuosity factor of the solid phase and pore phase are calculated using the *Taufactor* libraries [54]. The *Taufactor* is an open-source MATLAB application for efficiently calculating the tortuosity factor, as well as volume fractions, and specific surface areas, from image based

Table 2
The architecture of the 2D discriminator.

Layer	Kernel size	Stride	Padding	Output shape
Input	–	–	–	64 × 64 × 2
1	4	2	1	32 × 32 × 64
2	4	2	1	16 × 16 × 128
3	4	2	1	8 × 8 × 256
4	4	2	1	4 × 4 × 512
5	4	2	0	1 × 1 × 1

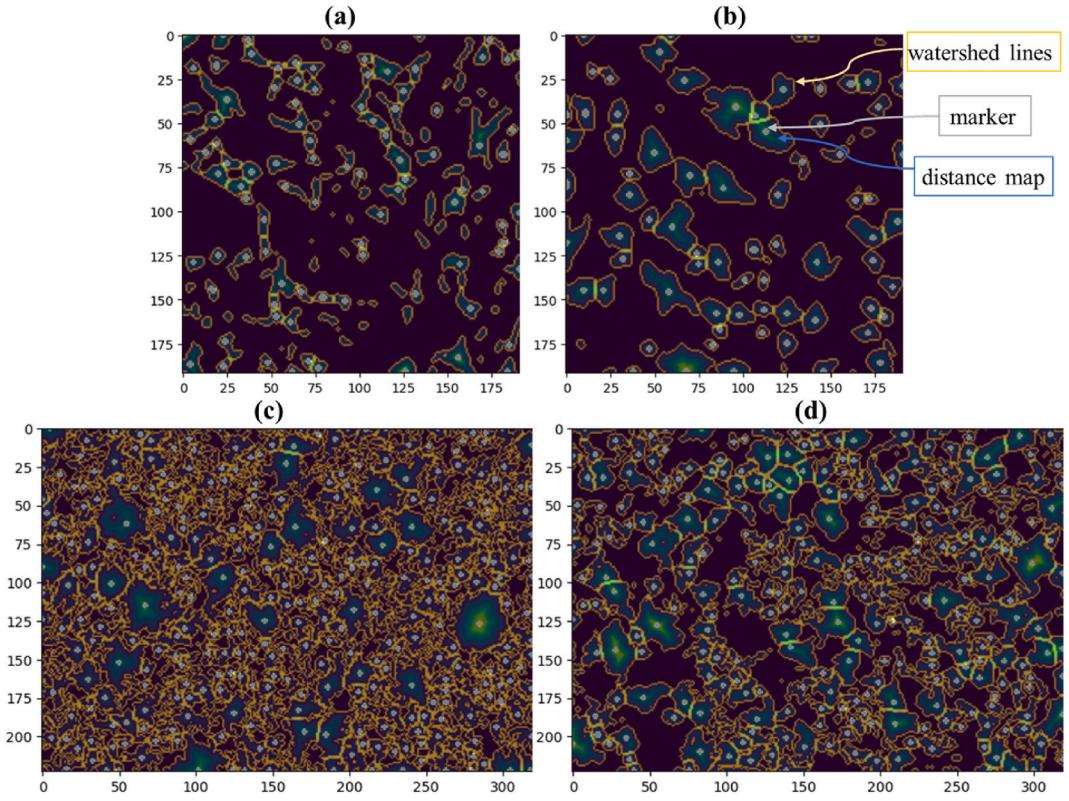

Fig. 4. Demonstration of SNOW-based pore segmentation of 2D porous images: (a) sample SOFC #1; (b) sample SOFC #2; (c) sample GV #1; and (d) sample GV #2. During the segmentation of all these images, the *r* is set to 2 pixels, and the *sigma* is set to 0.1.

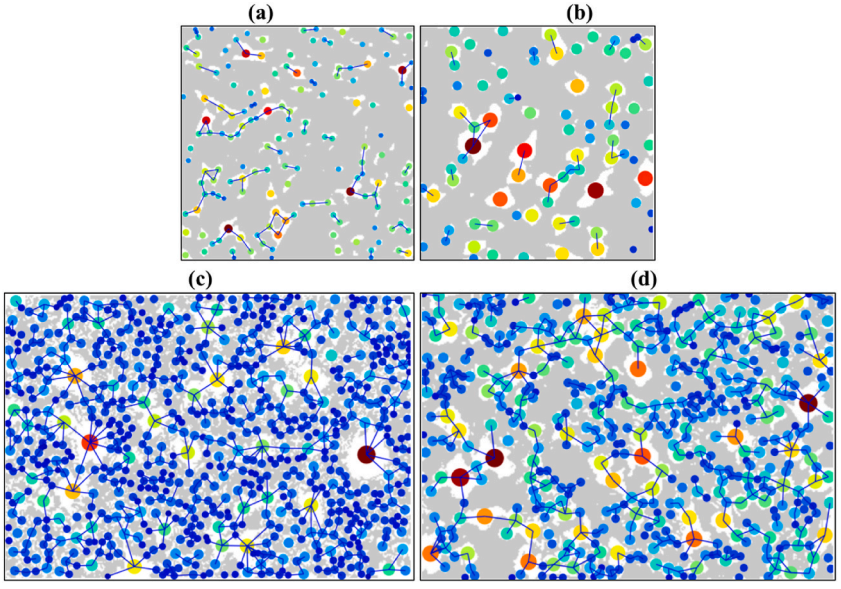

Fig. 5. Pore percolation in 2D microstructures with the Pore Network Model: (a) sample SOFC #1; (b) sample SOFC #2; (c) sample GV #1; and (d) sample GV #2. During the segmentation of all these images, the *r* is set to 2 pixels, and the *sigma* is set to 0.1.

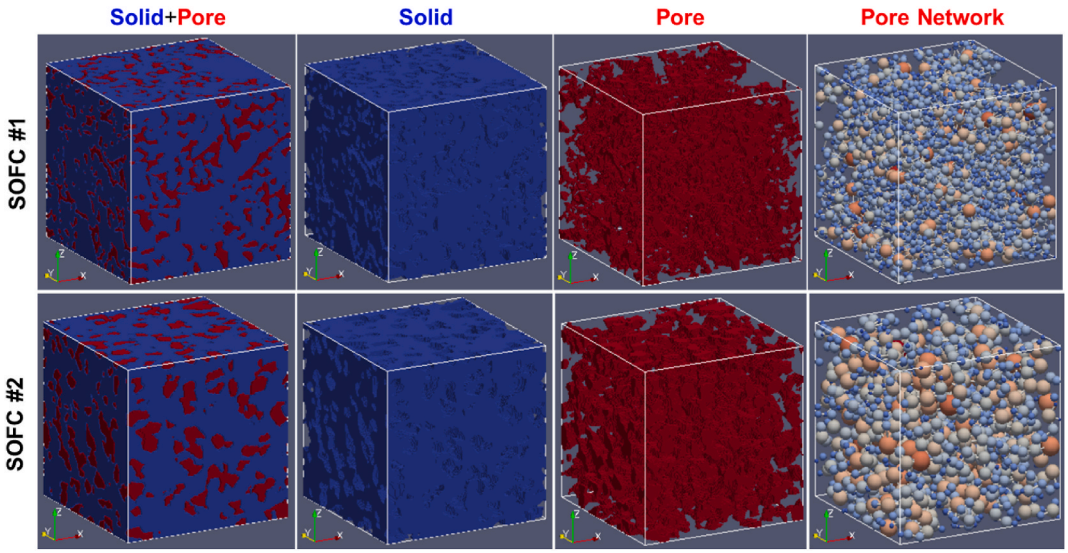

Fig. 6. Pore percolation in 3D microstructures and the sphere-stick network in Pore Network Model.

microstructural data. This tool calculates tortuosity factor using an over relaxed finite-different approach, allowing a fast computation for typical modern tomographic datasets as well as synthesized digital 3D image stacks.

2.5. Pore analysis with mercury intrusion porosimetry (MIP)

The mercury intrusion porosimetry (MIP) method is used to determine the pore size distribution and tortuosity factor of porous samples GV #1 and #2. Mercury is non-wetting to most solids, which means it does not wet solid surfaces. However, under pressure, mercury can intrude into the pores of a porous material. The relationship between the pressure and capillary diameter is described by Washburn [55] as:

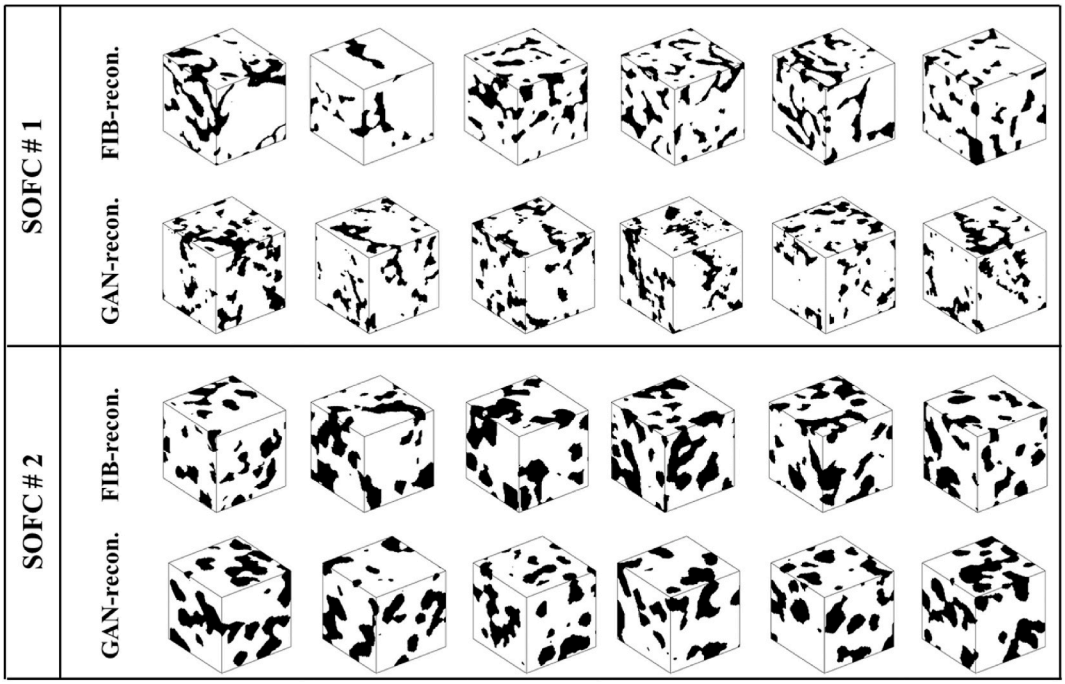

Fig. 7. 3D microstructure reconstruction of SOFC porous ceramic samples with the FIB-SEM and GAN methods.

$$P = \frac{-4\gamma \cos\theta}{D} \tag{1}$$

where P is the applied intrusion pressure, γ is the surface tension of the liquid, θ is the contact angle of the liquid, and D is the diameter of the capillary. In the formula, γ and θ are set to 0.480 N/m and 140°, respectively, in the mercury intrusion experiment. By measuring the volume of mercury intruded at different pressures, it is possible to determine the pore size distribution of the porous material. Larger pores will fill at lower pressures, while smaller pores will fill at higher pressures. The total volume of mercury intruded at a sufficiently high pressure is equal to the total pore volume of the material. This includes the volume of all the interconnected pores within the sample.

An AutoPore IV 9500 automatic mercury porosimeter (Micromeritics Instruments Co., GA, UAS) was used for the MIP experiment. The maximum mercury infiltration pressure is up to 414 MPa, and the range of pore diameter measurement is from 3 nm to about 350 μm.

3. Results and discussion

3.1. 3D reconstruction with FIB-SEM and GAN

Fig. 7 shows the 3D visualization of the reconstructed subvolumes of 64 × 64 × 64 voxels for samples SOFC #1 and #2 based on the FIB-SEM and the GAN reconstruction methods. It can be observed that there is no noticeable difference between the microstructures obtained with the two methods for both samples.

Although Fig. 7 only shows the subvolumes of 64 × 64 × 64 voxels of GAN reconstructed microstructures, much larger volumes can be generated with the trained generators $G(\boldsymbol{z})$ as long as the computational source permits. Fig. 8 shows GAN-generated cubic volumes with an edge length increasing from 64 voxels to 320 voxels using the trained generator based on 2D image data of sample SOFC #2 (see Fig. 9).

With the same GAN architecture for the SOFC samples, GANs were trained using the 2D images of *Geekvape* (GV) samples GV #1 and GV #2. Fig. 8 shows the GAN-generated 3D two-phase microstructures of samples GV #1 and GV #2. It can be seen that the GAN method can capture the diverse pore features in porous ceramics GV #1 and #2 which have a wide size distribution range and the volume equivalent spheres of the pores are displayed by the PMN model with the openPMN package [45].

In order to make a fair comparison between the FIB-SEM and GAN reconstructed 3D microstructures, microstructural metrics such as volume fraction, specific surface area, and tortuosity factor should be calculated based on the suitable representative volume of the sample. To this end, the size of the representative volume element (RVE) was analyzed first by evaluating the abovementioned microstructural metrics while varying the edge length of the sub-volume from 32 pixels to 192 pixels. The edge length is limited to a maximum of 192 pixels due to the limited volume obtained with the FIB-SEM reconstruction in the current study. Fig. 10 shows the statistics of the microstructural metrics for subvolumes with varied edge lengths for two SOFC samples which have different porosities and pore distributions. It is observed that for sample SOFC #1, an RVE size of 128 voxels allows the measurement of the volume fraction of solid and pore phases to be representative of the entire sample with an acceptable relative standard deviation within 5 % (Fig. 10(a)). For measurement of the specific surface area, it requires about 160 voxels for samples SOFC #1 to estimate the specific surface area with a relative standard deviation of about 5 % (Fig. 10(b)). For tortuosity factor measurements, an RVE size of 160 voxels allows the tortuosity factor of both the solids and pores of sample SOFC #1 (Fig. 10(c)) to be measured accurately.

For sample SOFC #2, it requires an RVE size of 96 pixels to allow the measurement of the volume fraction and specific surface area to be representative with an acceptable relative standard deviation within 5 % (Fig. 10 (d) and 10 (e)). For the tortuosity factor of the pores, it is forecasted that a larger RVE size of over 192 voxels is needed to represent the true value for the entire sample (Fig. 10(f)). Although the porosity in SOFC #2 is higher than that in SOFC #1, the pores in SOFC #2 are more likely isolated, causing a large

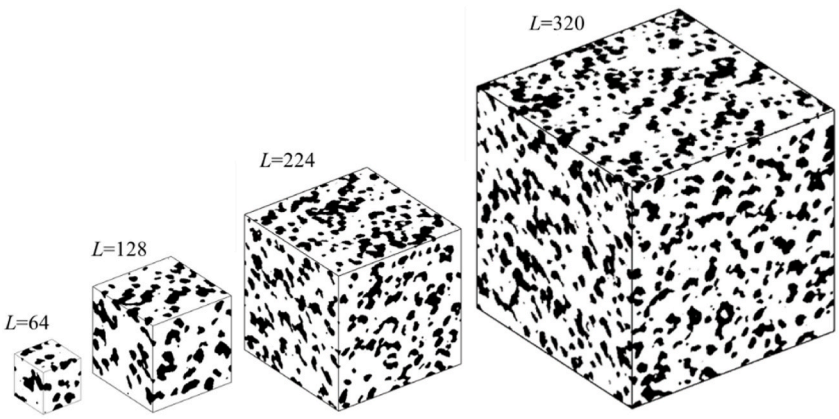

Fig. 8. GAN-reconstructed 3D microstructure of sample SOFC #2 with different volumes.

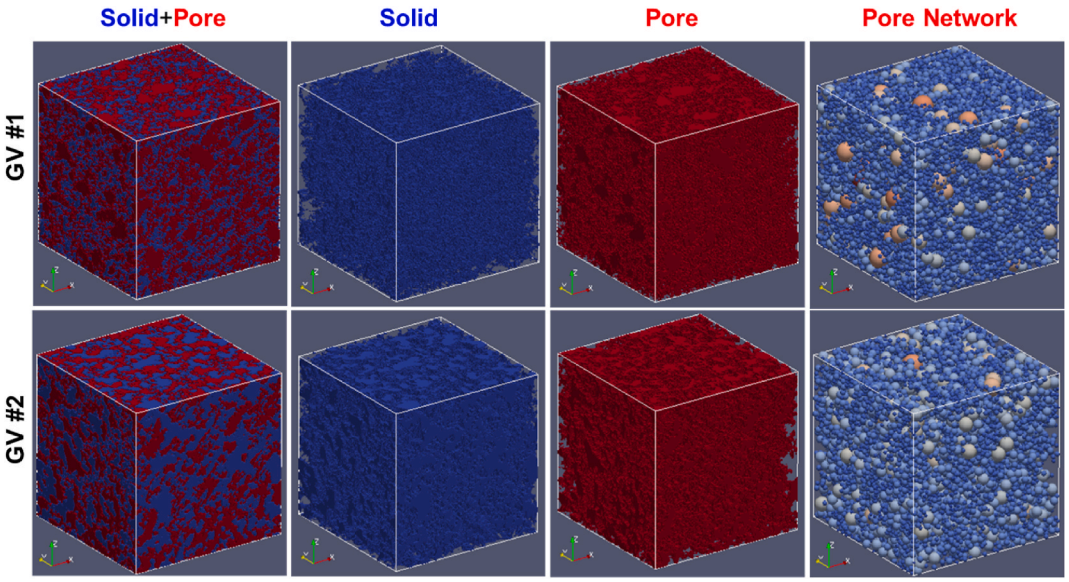

Fig. 9. The GAN-generated 3D microstructures and the PNM extracted using the openPMN tool [45] for samples GV #1 and #2.

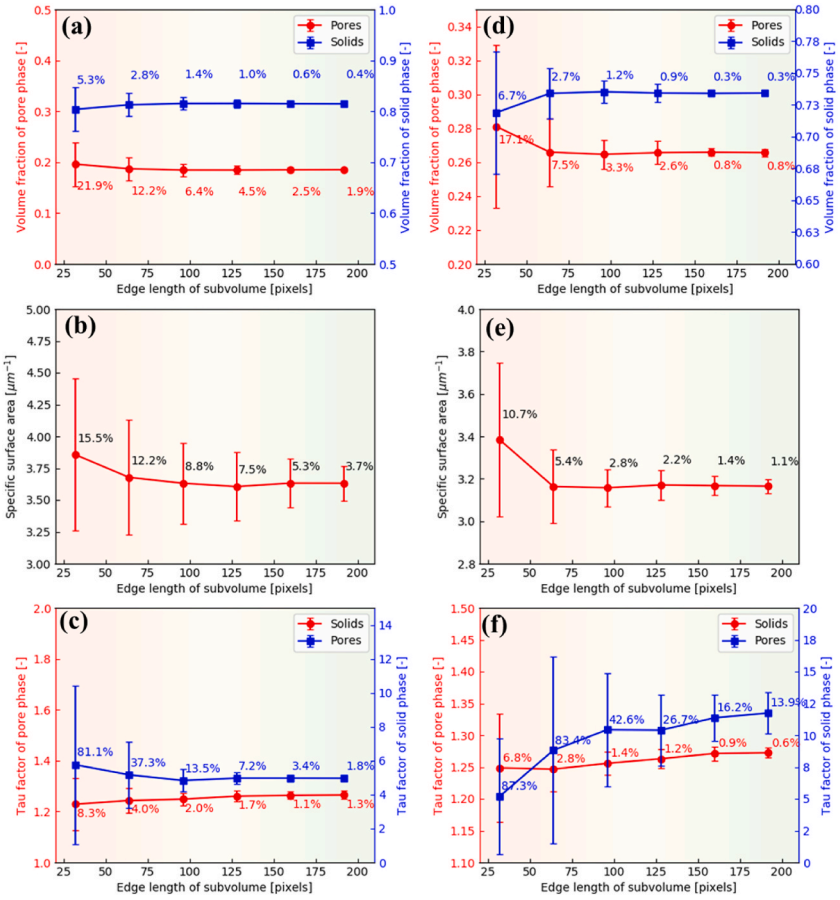

Fig. 10. RVE size analysis for the reconstructed 3D volumes of samples SOFC #1 and SOFC #2.

uncertainty of tortuosity factor measurement. This explains that a larger RVE size is required for SOFC #2 to analyze the tortuosity factor of pores.

In the current study, an RVE size of 192 voxels is determined suitable to evaluate all the microstructural metrics of the microstructures obtained by the FIB-SEM reconstruction and the GAN reconstruction methods for the two samples. Except for the measurement of the tortuosity factor of the pores in SOFC #2, all the other microstructural metrics of the two samples can be reliably represented.

Spatial correlation functions are widely used to characterize the heterogeneity of porous materials. In this study, the two-point correlation function [56], $S_2(r)$, was employed to compare the porous microstructure reconstructed using the GAN method with the real microstructure obtained from FIB-SEM reconstruction. The $S_2(r)$ values were calculated based on 20 random subvolumes, each of size 192 × 192 × 192 voxels, from both the FIB and GAN-reconstructed volumes. For the FIB reconstructed volumes, the 20 subvolumes are cut from the entire sample without overlapping volumes between two subvolumes, except for some small overlapping for subvolumes with an edge length larger than $L = 64$ pixels. Meanwhile, for the GAN-generated subvolumes, the 20 subvolumes are randomly generated from the same generator $G(\boldsymbol{z})$. As shown in Fig. 11, the pore characteristics of the GAN-reconstructed microstructures are in good agreement with those of the real microstructure in terms of $S_2(r)$ for samples SOFC #1 (Fig. 11(a)) and #2 (Fig. 11(b)).

Fig. 12 shows the boxplots of the five microstructural metrics' statistics carried out for the same 20 distinct subvolumes of 192 × 192 × 192 voxels of FIB and GAN reconstructed volumes previously used for the $S_2(r)$ measurements for samples SOFC #1 (Fig. 12(a)) and #2 (Fig. 12(b)). It is observed that for the two different samples, the volume fraction of the phases, specific surface area, and tortuosity factor of the solid phase of the 3D microstructures obtained with the two methods are in good consistency. For the tortuosity factor of the pores, there is a significant discrepancy. This discrepancy is possibly caused by the fact that the current RVE size is not sufficiently large for accurate statistics of the tortuosity factor of pore phase.

Fig. 13 shows the radar plot for the error analysis for the five microstructural metrics for the GAN-generated microstructure, with the measurement based on the FIB-SEM reconstructed microstructure as the ground truth. It is seen that the volume fraction of solids and pores, the specific surface area, and the tortuosity factor of the solid phase can be reproduced within errors of less than 5 % for the sample SOFC #1 and the tortuosity factor of pores is reproduced within an error of about 7.5 %. For the sample SOFC #2 only the volume fraction of solids and pores, the specific surface area, and the tortuosity factor of the solids can be reproduced within an error of 2.5 %. But for the tortuosity factor of the pores, the error is about 17.5 %. Again, by the definition of the error, this is simply because of the large deviation due to the limited RVE size for analysis. So, by and large, the GAN-generate microstructures have a very good quantitative agreement with the realistic microstructure which can be obtained from FIB-SEM reconstruction.

3.2. Analysis of pores based on 2D and 3D microstructures

Based on 2D images (20 slices of FIB-SEM cross-sections) and FIB reconstructed 3D image, the SNOW algorithm, with marker size controlling parameters $r = 2$ pixels and *sigma* = 0.2, was applied to both the 2D and 3D images for samples SOFC #1 and #2. Statistics in pore size distribution were carried out based on the volume-equivalent pore diameter of all segmented pores. The volume fraction and cumulative volume fraction distribution curves of the pore sizes measured on 2D and 3D images of samples SOFC #1 (Fig. 14(a)) and #2 (Fig. 14(b)) are shown in Fig. 14 for samples. It is seen that for both samples, the volume fraction and cumulative volume fraction distribution curves of the pore size distribution for 3D microstructure shift in the right direction (larger pore size) compared to those for the 2D microstructure. This means the D50 values of the pore size measured on the 2D microstructures are underestimated compared to those measured on the 3D microstructures. Yang et al. [57] measured the pore size of a die-cast AM60 material based on 2D and 3D microstructures by X-ray CT and also found the pore size peak of the 3D measurement was shifted to a larger size compared to that of the 2D measurement. The main reason for this size shift is the sectioning effect. For example, if we randomly section a sphere with a plane, the average diameter measured on the sectioned circle is about 2/3 of the sphere diameter. In practice, when researchers measure the grain size from 2D cross-sectional SEM images, the true 3D grain size is usually corrected by multiplying a scaling factor of 1.5 [58]. In addition, in 3D space, the pores are more likely to percolate than in a 2D cross-section and extra smaller pores can be

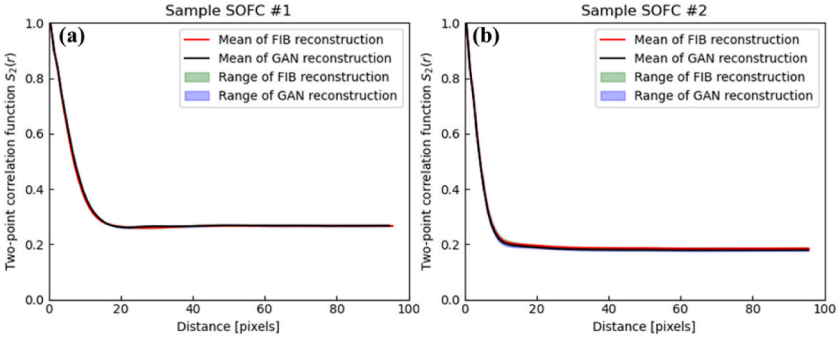

Fig. 11. Comparisons of the two-point correlation function of the FIB and the GAN reconstructed microstructures for (a) sample SOFC #1 and (b) sample SOFC #2.

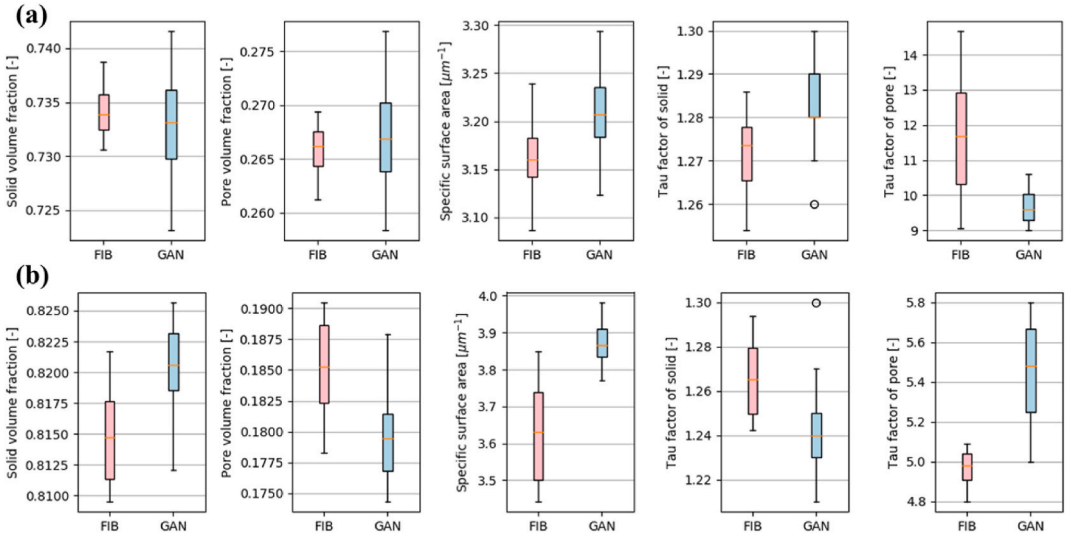

Fig. 12. Comparisons of the microstructural metrics obtained with the FIB reconstruction and the GAN reconstruction of (a) sample SOFC #1 and (b) sample SOFC #2.

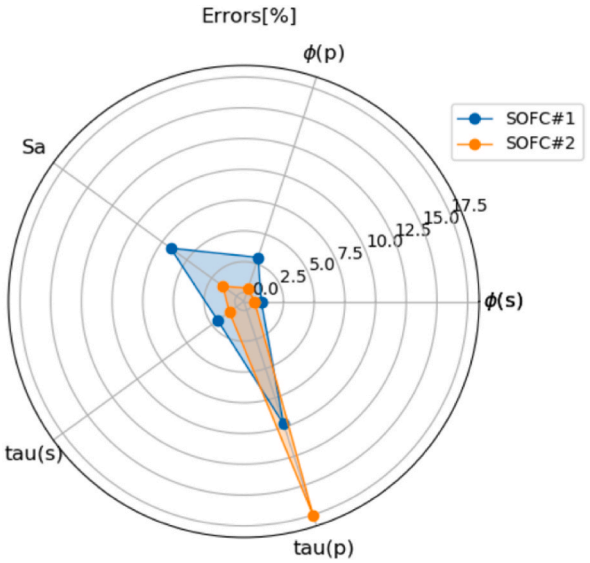

Fig. 13. Accuracy analysis on the GAN-based 3D reconstruction.

resulted after sectioning. As a consequence, in addition to the sectioning effect, 2D characterization can overestimate the pore population of small pores. Thus, the small pores count for a larger volume fraction of pores, resulting in a smaller D50 size for the 2D characterization. In other words, the characterization of pore sizes in 3D is believed to be more accurate than 2D characterization.

Besides the discrepancies in the microstructural metrics based on 2D and 3D microstructures, the actual diffusion behavior can also differ significantly. To demonstrate the necessity of considering 3D microstructures for diffusion problems, diffusions in solid and pore phases in 2D and 3D microstructures were conducted using the Taufactor libraries. It is evident that, for the two SOFC samples, only the solid phase percolates (Fig. 15 (b) and (h)), and the flux density along the solid phase in the 2D plane (Fig. 15 (c) and (h)) is very weak. In contrast, there is no percolation of the pores (black regions in Fig. 15 (a) and (f)) and no flux density in the pore phase at all. In the case of the 3D microstructures, there are higher flux densities for both the solids (Fig. 15 (d) and (i)) and pores (Fig. 15 (e) and (j)) compared to the 2D simulations. Hu et al. [59] performed direct comparisons between the transfer coefficient based on 2D and 3D porous models of packed beds which were obtained by X-ray CT scanning. They found that the overall mass transfer coefficient was higher in the 3D-packed bed under Darcy flow conditions. Similarly, Stec et al. [60] calculated the permeability of 2D and 3D microstructures and they significantly differed. They found that the permeability calculated for 2D models strongly depended on the 2D slice chosen for the calculation. The more reliable results were obtained when several 2D slices were investigated.

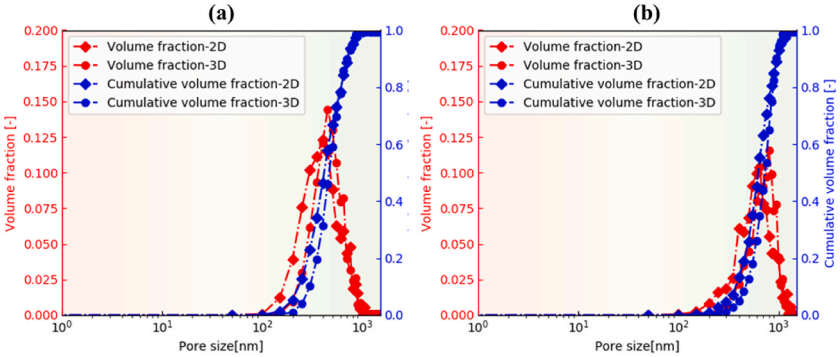

Fig. 14. Pore size distribution in two porous ceramic samples based on the 2D and 3D microstructures: (a) Sample SOFC #1 and (b) sample SOFC #2.

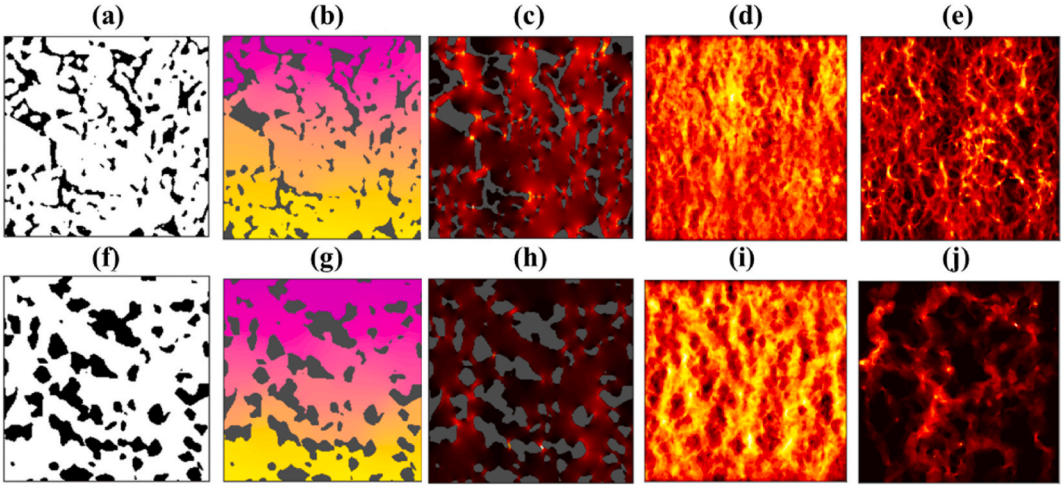

Fig. 15. The simulated flux densities in the 2D and 3D microstructures of samples SOFC #1 and SOFC #2: (a) and (f) microstructures with white regions as solids and the black as pores; (b) and (g) the effectively percolated solid phase; (c) and (h) the simulated flux density in the solid phase of the 2D microstructures; (d) and (i) projections of the flux densities in the solid phase of the 3D microstructures; (e) and (j) projections of the flux densities in the pore phase of the 3D microstructures.

For sample GV #1, with a porosity of 0.60 measured from the binary image (Fig. 16(a)), which is significantly higher than that of samples SOFC #1 and #2, the pores are shown to be percolated in the 2D plane, as illustrated in Fig. 16(b). The diffusion simulation reveals a very weak flux density in the pore phase within the 2D plane, as depicted in Fig. 16(c). However, in the GAN-reconstructed 3D microstructure (Fig. 16(d)), the pore phase displayed in the 2D plane is effectively interconnected in 3D space (Fig. 16(e)), resulting in significantly higher flux density in the 3D space (Fig. 16(f)). Similarly, in sample GV #2 (Fig. 17), with a porosity of approximately 0.50, the pores in the 2D plane are also interconnected from one side to another (Fig. 17(a) and (b)), leading to flux within the 2D plane (Fig. 17(c)). In the GAN reconstructed 3D microstructure, the pore percolation (Fig. 17(d) and (e)) and flux (Fig. 17(f)) density are both increased. The percolation of the solid phase is very similar to those in the samples SOFC #1 and #2 and is not discussed here.

Based on the flux simulations using both 2D and 3D microstructures of porous media with varying densities and pore characteristics, as seen in typical SOFC electrode materials (SOFC #1 and #2) and ceramic atomizer core materials (GV #1 and GV #2), the conclusions drawn from 2D and 3D results can be significantly different. For materials with critical porosity, pores may appear disconnected in 2D images, while they are actually interconnected in the 3D space. Consequently, image-based simulations relying solely on 2D microstructures can lead to unreliable predictions of physical properties, such as permeability, mechanical strength, electrical, or thermal conductivity. Therefore, it is essential to access the full 3D microstructure of porous media to accurately investigate these material properties. The proposed GAN method can recover missing information by reconstructing the 3D microstructure from 2D microstructures and may be beneficial for predicting macroscopic properties of materials from 2D images.

3.3. Comparison with the MIP method

Although the MIP method can measure pore sizes in the range of 3 nm–350 μm, the measurement of nanometric pores is, in fact, not

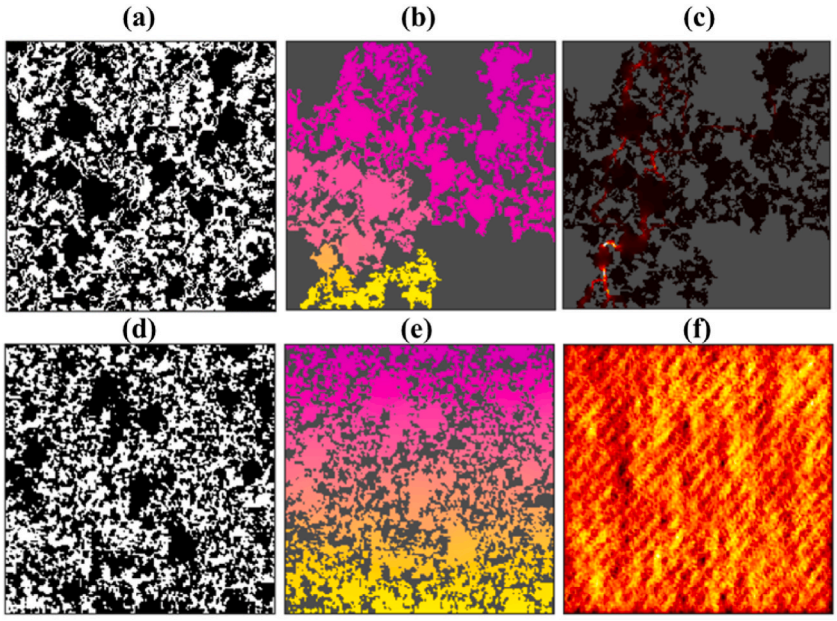

Fig. 16. The simulated flux densities in the 2D and GAN-generated 3D microstructures of the sample GV #1: (a) the 2D binary microstructure from SEM and (d) 2D slice from GAN-generated 3D microstructures with white regions as solids and the black as pores; (b) and (e) the effectively percolated solid phase in 2D and 3D microstructures; (c) and (f) the simulated flux density in the pore phase of the 2D and 3D microstructures.

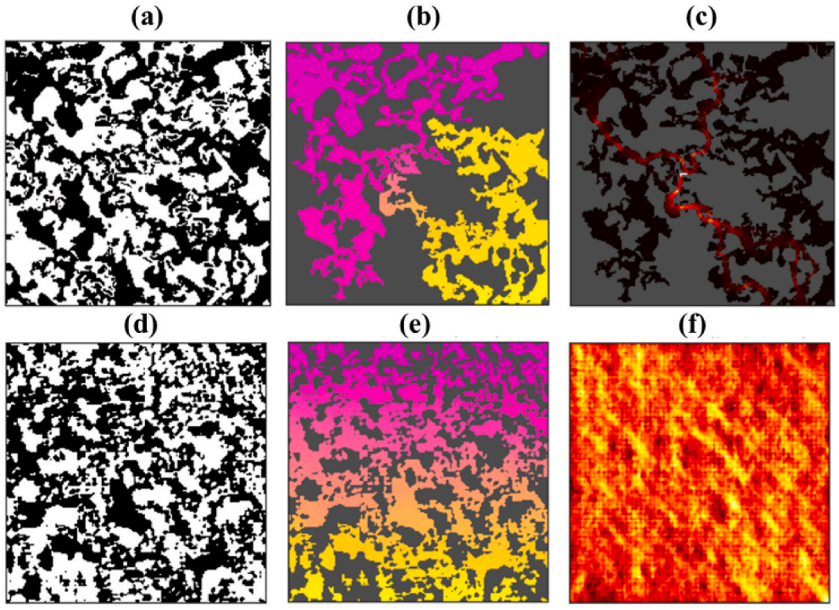

Fig. 17. The simulated flux densities in the 2D and GAN-generated 3D microstructures of the sample GV #2: (a) the 2D binary microstructure from SEM and (d) 2D slice from GAN-generated 3D microstructures with white regions as solids and the black as pores; (b) and (e) the effectively percolated solid phase in 2D and 3D microstructures; (c) and (f) the simulated flux density in the pore phase of the 2D and 3D microstructures.

accurate. This inaccuracy arises because, in order to access the fine pores, mercury needs to be subjected to high intrusion pressure, causing the collapse of the smaller pores and resulting in measured values that deviate from the actual values. As shown in Fig. 18, the volume fraction and cumulative volume fraction curves of the pore size distribution in samples GV #1 (Fig. 18(a)) and #2 (Fig. 18(b)) exhibit a log-normal distribution. For GV #1, the D50 size of the pores is approximately 10 μm, while for GV #2, the D50 size of the pores is slightly larger, measuring around 20 μm.

In this study, the pore analysis of GAN-reconstructed samples GV#1 and GV#2 is sensitive to the SNOW segmentation algorithms,

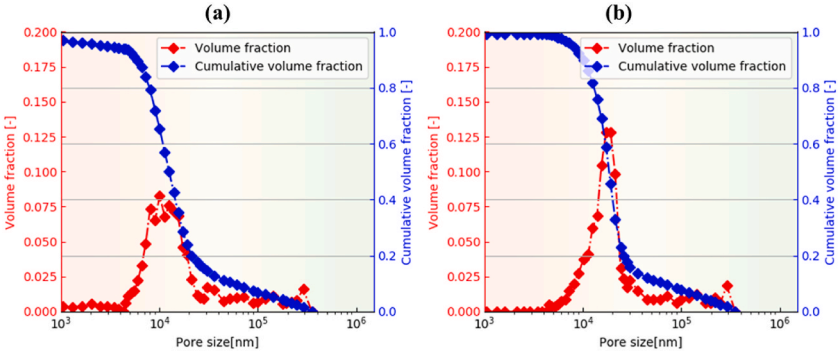

Fig. 18. Pore size distribution in two porous ceramic samples based on the MIP method: (a) Sample GV#1 and (b) sample GV#2.

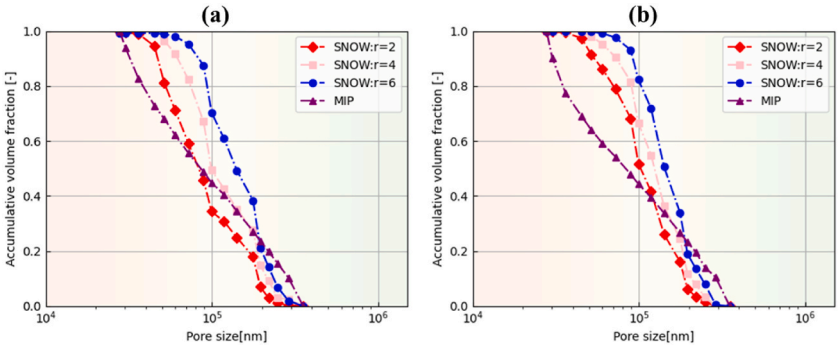

Fig. 19. Pore size distribution (accumulative probability density) in two porous ceramic samples based on the MIP method: (a) Sample GV#1 and (b) sample GV#2.

particularly the marker size (parameter r) and Gaussian filtering levels (parameter sigma). In the previous section on the SEM characterization of microstructures GV#1 and GV#2, the image resolution is approximately 3 μm per pixel, effectively capturing pore sizes at the scale of a few microns. In the case of GV samples, the smallest pore size, as determined by the SNOW segmentation algorithm, is approximately 20 μm. To compare the pore size distribution obtained by the image-based method and the MIP method, pores in the size range of 20–350 μm are considered, and the distribution density function is recalculated for the MIP results for samples GV #1 (Fig. 19(a)) and GV #2 (Fig. 19(b)).

It is observed that as the marker size (r values) increases, the pore networks are consolidated into fewer regions, resulting in a smaller volume ratio of small pores and a larger volume ratio of larger pores. This indicates that pore size statistics based on the SNOW algorithm depend on segmentation parameters and require experimental data for calibration. For both samples, a SNOW-based pore segmentation with a marker size parameter of $r = 4$ pixels approximates the MIP results for larger pores (100–350 μm). However, for smaller pore segmentation, a marker size parameter of $r = 4$ pixels appears to cause under-segmentation of the pores, resulting in insufficient separation of the network of smaller pores and leading to discrepancies in the pore size distribution within the range of 20–100 μm. This suggests that the SNOW algorithm has limitations when being applied to porous microstructures which have a wide

Table 3
Comparison of microstructural metrics measurements based on 2D, and 3D microstructures and based on the MIP experiments. 3D microstructures of the SOFC samples and the GV samples are FIB-SEM reconstructed and GAN reconstructed, respectively.

Samples and methods		Volume fraction of pores φ(p)/-	Volume fraction of pores φ(s)/-	Specific surface area S_a/μm^{-1}	Tortuosity factor of pores *tau*(p)/-	Tortuosity factor of solids *tau*(s)/-
SOFC #1	2D	0.182 ± 0.017	0.818 ± 0.017	–	INF	1.748 ± 0.276
	3D	0.185 ± 0.003	0.815 ± 0.003	3.628 ± 0.136	4.961 ± 0.090	1.265 ± 0.016
SOFC #2	2D	0.268 ± 0.018	0.732 ± 0.018	–	INF	1.777 ± 0.159
	3D	0.266 ± 0.002	0.734 ± 0.002	3.163 ± 0.035	11.422 ± 2.161	1.272 ± 0.008
GV #1	2D	0.593 ± 0.003	0.407 ± 0.004	–	22.6 ± 5.349	INF
	3D	0.597 ± 0.005	0.403 ± 0.005	0.170 ± 0.001	2.044 ± 0.018	3.120 ± 0.056
	MIP	0.598	0.402	–	1.554	–
GV #2	2D	0.487 ± 0.007	0.513 ± 0.007	–	21.846 ± 3.723	INF
	3D	0.491 ± 0.003	0.509 ± 0.003	0.109 ± 0.024	2.245 ± 0.032	2.482 ± 0.026
	MIP	0.488	0.512	–	1.678	–

distribution of pore size and may require a variable marker size parameter.

Alternatively, researchers have developed numerical mercury intrusion porosimetry (MIP) based on 3D porous microstructures. In this study, one ongoing challenge is the wide range of pore size distribution, spanning from a few nanometers to hundreds of microns. High-resolution microstructure acquisition presents challenges for the current experimental techniques with FIB-SEM and X-ray tomography. Another remaining issue is that even if high-resolution 2D microstructures are attainable, training the GAN model requires large input images, leading to computational challenges.

Finally, we compared the measurement results of the microstructural metrics based on 2D microstructures from SEM, the results based on 3D microstructures with FIB-SEM and GAN reconstruction, as well as the results obtained through the MIP experiment method (only available for samples GV #1 and #2). A summary is presented in Table 3.

For the volume fraction of the pores (also known as porosity), the 2D and 3D measurements, along with MIP data, provide very close results. However, specific surface area cannot be directly measured from the 2D microstructures. Technically, the tortuosity factor of a specific phase can be calculated based on both 2D and 3D images. Nevertheless, the 2D results cannot represent the true values, particularly when the volume/areal fraction is lower than the critical percolation value, resulting in an infinite tortuosity factor.

For samples SOFC #1 and #2, where the porosity is very low and the pores in 2D planes are not percolated, the tortuosity factor becomes infinite. Similarly, for samples GV #1 and #2, where the porosity is high and the pores are percolated, the tortuosity factor can be calculated, while the solid phase is not percolated, resulting in an infinite tortuosity factor of solids. However, for both the SOFC and GV samples, the tortuosity factors of the pores and solids can be calculated based on 3D microstructures.

Furthermore, through the direct comparison of the tortuosity factor of pores based on the GAN-generated 3D microstructure and the MIP-measured data for samples GV #1 and #2, good agreement is observed, demonstrating the promise of tortuosity factor calculations based on GAN-generated microstructures. Nevertheless, caution should be exercised when evaluating the tortuosity factor or transportation phenomena in porous ceramic devices solely based on 2D microstructural metrics. If these metrics are used for further modeling, such as multiphysics modeling of electrochemical reactions in SOFC electrodes, the final predictions can be highly questionable.

4. Conclusions

In this study, we employed a GAN-based deep learning method to reconstruct the 3D microstructures of porous ceramic materials from 2D cross-sectional microstructures. Quantitative comparisons between the GAN-reconstructed and FIB-SEM-reconstituted realistic porous samples demonstrate excellent agreement in capturing parameters such as volume fraction, specific surface area, and tortuosity factors. Our 2D and 3D study underscores the necessity of utilizing 3D microstructures to access certain critical microstructural metrics, including tortuosity factors, pore size, and pore size distribution, although the volume fraction of phases can be recovered accurately from the 2D microstructures. These microstructural metrics hold significant importance when addressing numerical simulations for porous devices, such as electrochemical reactions and heat and mass transfer in the porous electrodes of fuel cells and other energy conversion and storage devices. By combining the GAN reconstruction and numerical simulations, pore size, and tortuosity information can be estimated as an alternative to the mercury intrusion porosimetry method.

CRediT authorship contribution statement

Xianhang Li: Writing – original draft, Validation, Methodology, Investigation, Formal analysis, Data curation. **Shihao Zhou:** Writing – review & editing, Methodology, Investigation. **Xuhao Liu:** Visualization, Software. **Jiadong Zang:** Writing – review & editing, Resources. **Wenhao Fu:** Writing – review & editing, Resources. **Wenlong Lu:** Writing – review & editing, Resources. **Haibo Zhang:** Writing – review & editing, Supervision, Methodology. **Zilin Yan:** Writing – review & editing, Supervision, Resources, Project administration, Conceptualization.

Data availability statement

Data will be made available on request.

Declaration of competing interest

The authors declare that they have no known competing financial interests or personal relationships that could have appeared to influence the work reported in this paper.

Acknowledgements

This work was supported by the National Natural Science Foundation of China (No. 12172104), the Stable Supporting Fund of Shenzhen (GXWD20231130153335002), the Talent Recruitment Project of Guangdong (2021QN02L892), Shccig-Qinling Program (SMYJY202300140C), the Program of Innovation Team in Universities and Colleges in Guangdong (2021KCXTD006), Shenzhen Science and Technology Innovation Commission (JCYJ20200109113439837) and Development and Reform Commission of Shenzhen (XMHT20220103004).

References

[1] N. Hedayat, Y. Du, H. Ilkhani, Review on fabrication techniques for porous electrodes of solid oxide fuel cells by sacrificial template methods, Renew. Sustain. Energy Rev. 77 (2017) 1221–1239, https://doi.org/10.1016/j.rser.2017.03.095.

[2] Z. Chen, D.L. Danilov, R.-A. Eichel, P.H.L. Notten, Porous electrode modeling and its applications to Li-Ion batteries, Adv. Energy Mater. 12 (2022) 2201506, https://doi.org/10.1002/aenm.202201506.

[3] A. Maghfirah, M.M. Ilmi, A.T.N. Fajar, G.T.M. Kadja, A review on the green synthesis of hierarchically porous zeolite, Mater. Today Chem. 17 (2020) 100348, https://doi.org/10.1016/j.mtchem.2020.100348.

[4] D. Li, H.-Q. Xu, L. Jiao, H.-L. Jiang, Metal-organic frameworks for catalysis: state of the art, challenges, and opportunities, Energychem 1 (2019) 100005, https://doi.org/10.1016/j.enchem.2019.100005.

[5] Z. Chen, K.O. Kirlikovali, K.B. Idrees, M.C. Wasson, O.K. Farha, Porous materials for hydrogen storage, Chem 8 (2022) 693–716, https://doi.org/10.1016/j.chempr.2022.01.012.

[6] D.S. Ahmed, G.A. El-Hiti, E. Yousif, A.A. Ali, A.S. Hameed, Design and synthesis of porous polymeric materials and their applications in gas capture and storage: a review, J. Polym. Res. 25 (2018) 1–21, https://doi.org/10.1007/s10965-018-1474-x.

[7] Y. Liu, Y. Bai, T. Tian, Preparation of porous liquid based on silicalite-1, Materials 12 (2019) 3984, https://doi.org/10.3390/ma12233984.

[8] H. Zhang, H. Gao, X. Liu, H. Yu, L. Wang, Y. Jiang, L. Gao, L. Yu, Y. He, X. Chen, L. Zhang, G. Zheng, Reactive synthesis and assessment of porous Fe-20.5Al-18Cr intermetallic material: a comparative study with porous FeCrAl material produced from prealloyed powders, Sep. Purif. Technol. 220 (2019) 152–161, https://doi.org/10.1016/j.seppur.2019.03.054.

[9] J. Xiao, J. Liang, C. Zhang, Y. Tao, G.-W. Ling, Q.-H. Yang, Advanced materials for capturing particulate matter: progress and perspectives, Small Methods 2 (2018) 1800012, https://doi.org/10.1002/smtd.201800012.

[10] R. Li, W. Yang, S. Gao, J. Shang, Q. Li, Hydrous cerium oxides coated glass fiber for efficient and long-lasting arsenic removal from drinking water, J. Adv. Ceram. 10 (2021) 247–257, https://doi.org/10.1007/s40145-020-0435-0.

[11] T.A. Esquivel-Castro, M.C. Ibarra-Alonso, J. Oliva, A. Martinez-Luevanos, Porous aerogel and core/shell nanoparticles for controlled drug delivery: a review, Mater. Sci. Eng. C-Mater. Biol. Appl. 96 (2019) 915–940, https://doi.org/10.1016/j.msec.2018.11.067.

[12] Y. Tang, A. Varyambath, Y. Ding, B. Chen, X. Huang, Y. Zhang, D.-G. Yu, I. Kim, W. Song, Porous organic polymers for drug delivery: hierarchical pore structures, variable morphologies, and biological properties, Biomater. Sci. 10 (2022) 5369–5390, https://doi.org/10.1039/d2bm00719c.

[13] Z. Liu, J. Lyu, D. Fang, X. Zhang, Nanofibrous kevlar aerogel threads for thermal insulation in harsh environments, ACS Nano 13 (2019) 5703–5711, https://doi.org/10.1021/acsnano.9b01094.

[14] M. Li, Z. Qin, Y. Cui, C. Yang, C. Deng, Y. Wang, J.S. Kang, H. Xia, Y. Hu, Ultralight and flexible monolithic polymer aerogel with extraordinary thermal insulation by a facile ambient process, Adv. Mater. Interfaces 6 (2019) 1900314, https://doi.org/10.1002/admi.201900314.

[15] L. Wang, Z. Cai, L. Su, M. Niu, K. Peng, L. Zhuang, H. Wang, Bifunctional SiC/Si_3N_4 aerogel for highly efficient electromagnetic wave absorption and thermal insulation, J. Adv. Ceram. 12 (2023) 309–320, https://doi.org/10.26599/JAC.2023.9220684.

[16] I. Sopyan, M. Mel, S. Ramesh, K.A. Khalid, Porous hydroxyapatite for artificial bone applications, Sci. Technol. Adv. Mater. 8 (2007) 116–123, https://doi.org/10.1016/j.stam.2006.11.017.

[17] D.W. Wang, F. Li, M. Liu, G.Q. Lu, H.M. Cheng, 3D aperiodic hierarchical porous graphitic carbon material for high-rate electrochemical capacitive energy storage, Angew. Chem.-Int. Edit. 47 (2008) 373–376, https://doi.org/10.1002/anie.200702721.

[18] J. Shao, C. Baia, X. Li, K. Yang, T. Zheng, Y. Qiao, L. Zhang, H. Li, P. Colombo, Open-cell mullite ceramic foams derived from porous geopolymer precursors with tailored porosity, J. Adv. Ceram. 12 (2023) 279–295, https://doi.org/10.26599/JAC.2023.9220682.

[19] R. Liu, L. Ma, H. Liu, B. Xu, C. Feng, R. He, Effects of pore size on the mechanical and biological properties of stereolithographic 3D printed HAp bioceramic scaffold, Ceram. Int. 47 (2021) 28924–28931, https://doi.org/10.1016/j.ceramint.2021.07.053.

[20] S.M. Miller, X. Xiao, J.A. Setlock, K.T. Faber, Freeze-cast alumina pore networks: effects of processing parameters in steady-state solidification regimes of aqueous slurries, J. Eur. Ceram. Soc. 38 (2018) 5134–5143, https://doi.org/10.1016/j.jeurceramsoc.2018.07.009.

[21] J. Zou, C. Fan, X. Liu, Effects of molecular cross-sectional areas of adsorbed nitrogen on the Brunauer-Emmett-Teller analysis for carbon-based slit pores, Langmuir 36 (2020) 14656–14665, https://doi.org/10.1021/acs.langmuir.0c02514.

[22] Y. Ma, G. Wang, G. Ye, J. Hu, A comparative study on the pore structure of alkali-activated fly ash evaluated by mercury intrusion porosimetry, N_2 adsorption and image analysis, J. Mater. Sci. 53 (2018) 5958–5972, https://doi.org/10.1007/s10853-017-1965-x.

[23] T. Saif, Q. Lin, A.R. Butcher, B. Bijeljic, M.J. Blunt, Multi-scale multi-dimensional microstructure imaging of oil shale pyrolysis using X-ray micro-tomography, automated ultra-high resolution SEM, MAPS Mineralogy and FIB-SEM, Appl. Energy 202 (2017) 628–647, https://doi.org/10.1016/j.apenergy.2017.05.039.

[24] F. Monaco, M. Hubert, J.C. Da Silva, V. Favre-Nicolin, D. Montinaro, P. Cloetens, J. Laurencin, A comparison between holographic and near-field ptychographic X-ray tomography for solid oxide cell materials, Mater. Charact. 187 (2022) 111834, https://doi.org/10.1016/j.matchar.2022.111834.

[25] L. Varoto, J.-J. Blandin, P. Lhuissier, S. Roure, A. Papillon, M. Chosson, G. Martin, 3D microstructure characterization of Cu25Cr solid state sintered alloy using X-ray computed tomography and machine learning assisted segmentation, Mater. Charact. 203 (2023) 113107, https://doi.org/10.1016/j.matchar.2023.113107.

[26] M. Čalkovský, E. Müller, M. Meffert, N. Firman, F. Mayer, M. Wegener, D. Gerthsen, Comparison of segmentation algorithms for FIB-SEM tomography of porous polymers: importance of image contrast for machine learning segmentation, Mater. Charact. 171 (2021) 110806, https://doi.org/10.1016/j.matchar.2020.110806.

[27] B. Chen, Z. Xia, K. Lu, Understanding sintering characteristics of ZnO nanoparticles by FIB-SEM three-dimensional analysis, J. Eur. Ceram. Soc. 33 (2013) 2499–2507, https://doi.org/10.1016/j.jeurceramsoc.2013.04.026.

[28] M. Atmaca, I. Girgin, C. Ezgi, CFD modeling of a diesel evaporator used in fuel cell systems, Int. J. Hydrog. Energy. 41 (2016) 6004–6012, https://doi.org/10.1016/j.ijhydene.2016.02.122.

[29] X. Li, L. Duan, S. Zhou, X. Liu, Z. Yao, Z. Yan, Freeze-casting of alumina and permeability analysis based on a 3D microstructure reconstructed using generative adversarial networks, Materials 17 (2024) 2432.

[30] D. Zhang, A. Forner-Cuenca, O.O. Taiwo, V. Yufit, F.R. Brushett, N.P. Brandon, S. Gu, Q. Cai, Understanding the role of the porous electrode microstructure in redox flow battery performance using an experimentally validated 3D pore-scale lattice Boltzmann model, J. Power Sources 447 (2020) 227249, https://doi.org/10.1016/j.jpowsour.2019.227249.

[31] Z. Yan, A. He, S. Hara, N. Shikazono, Modeling of solid oxide fuel cell (SOFC) electrodes from fabrication to operation: correlations between microstructures and electrochemical performances, Energy Convers. Manag. 190 (2019) 1–13, https://doi.org/10.1016/j.enconman.2019.04.002.

[32] X. Liu, S. Zhou, Z. Yan, Z. Zhong, N. Shikazono, S. Hara, Correlation between microstructures and macroscopic properties of nickel/yttria-stabilized zirconia (Ni-YSZ) anodes: meso-scale modeling and deep learning with convolutional neural networks, Energy AI 7 (2022) 100122, https://doi.org/10.1016/j.egyai.2021.100122.

[33] B. Zhang, H. Huang, S. Wu, W. Li, J. Huang, A. Lin, Q. Wu, Y. Liu, T. Xiao, In-situ X-ray tomography on permeability evolution of C/SiC porous ceramic for hypersonic vehicles, Ceram. Int. 47 (2021) 27770–27777, https://doi.org/10.1016/j.ceramint.2021.06.204.

[34] R.D. Hazlett, Statistical characterization and stochastic modeling of pore networks in relation to fluid flow, Math. Geol. 29 (1997) 801–822, https://doi.org/10.1007/bf02768903.

[35] L. Mosser, O. Dubrule, M.J. Blunt, Reconstruction of three-dimensional porous media using generative adversarial neural networks, Phys. Rev. E 96 (2017) 043309, https://doi.org/10.1103/PhysRevE.96.043309.

[36] M. Qian, J. Zhou, J. Wang, L. Ruan, Z. Xiang, X. Hu, Permeability prediction of complex porous materials by conjugating generative adversarial and convolutional neural networks, Comput. Mat. Sci. 238 (2024) 112942, https://doi.org/10.1016/j.commatsci.2024.112942.

[37] M. Kishimoto, Y. Matsui, H. Iwai, Conditional generative adversarial network for generation of three-dimensional porous structure of solid oxide fuel cell anodes with controlled volume fractions, J. Power Sources 580 (2023) 233411, https://doi.org/10.1016/j.jpowsour.2023.233411.
[38] R. Shams, M. Masihi, R.B. Boozarjomehry, M.J. Blunt, Coupled generative adversarial and auto-encoder neural networks to reconstruct three-dimensional multi-scale porous media, J. Pet. Sci. Eng. 186 (2020) 106794, https://doi.org/10.1016/j.petrol.2019.106794.
[39] R. Shams, M. Masihi, R.B. Boozarjomehry M.J. Blunt, A Hybrid of statistical and conditional generative adversarial neural network approaches for reconstruction of 3D porous media (ST-CGAN), Adv. Water Resour. 158 (2021) 104064, https://doi.org/10.1016/j.advwatres.2021.104064.
[40] F. Zhang, X. He, Q. Teng, X. Wu, X. Dong, 3D-PMRNN: reconstructing three-dimensional porous media from the two-dimensional image with recurrent neural network, Knowl-based Syst 264 (2023) 110333, https://doi.org/10.1016/j.petrol.2021.109652.
[41] Q. Zheng, D. Zhang, RockGPT: reconstructing three-dimensional digital rocks from single two-dimensional slice with deep learning, Comput. Geosci. 26 (2022) 677–696, https://doi.org/10.1007/s10596-022-10144-8.
[42] S. Kench, S.J. Cooper, Generating three-dimensional structures from a two-dimensional slice with generative adversarial network-based dimensionality expansion, Nat. Mach. Intell. 3 (2021) 299–305, https://doi.org/10.1038/s42256-021-00322-1.
[43] S. Zhou, X. Liu, Z. Yan, S. Hara, N. Shikazono, Z. Zhong, Kinetic Monte Carlo (KMC) simulation of sintering of nickel oxide-yttria stabilized zirconia composites: model, parameter calibration and validation, Mater. Des. 232 (2023) 112094, https://doi.org/10.1016/j.matdes.2023.112094.
[44] Z. Yan, O. Guillon, C.L. Martin, S. Wang, C.-S. Lee, F. Charlot, D. Bouvard, Correlative studies on sintering of Ni/$BaTiO_3$ multilayers using X-ray computed nanotomography and FIB-SEM nanotomograhy, J. Am. Ceram. Soc. 98 (2015) 1338–1346, https://doi.org/10.1111/jace.13416.
[45] A. Anantatamukala, K.V. Mani Krishna, Narendra B. Dahotre, Generative adversarial networks assisted machine learning based automated quantification of gain size from scanning electron microscope back scatter images, Mater. Charact. 206 (2023) 113396, https://doi.org/10.1016/j.matchar.2023.113396.
[46] G. Bianco, T. Paul, A. Nisar, A. Hamrani, B. Boesl, A. Agarwal, Nanoindentation mapping defects filtration for heterogeneous materials using generative adversarial networks, Mater. Charact. 191 (2022) 112107, https://doi.org/10.1016/j.matchar.2022.112107.
[47] E. Smith, D. Meger, Improved adversarial systems for 3D object generation and reconstruction, Preprint at, https://doi.org/10.48550/arXiv.1707.09557, 2017.
[48] S. Kench, S.J. Cooper, Generating three-dimensional structures from a two-dimensional slice with generative adversarial network-based dimensionality expansion, Nat. Mach. Intell. 3 (2021) 299–305, https://doi.org/10.1038/s42256-021-00322-1.
[49] D.P. Kingma, J. Ba, Adam: a method for stochastic optimization, Preprint at, https://arxiv.org/abs/1412.6980, 2014.
[50] Z. Yan, Y. Kim, S. Hara, N. Shikazono, Prediction of $La_{0.6}Sr_{0.4}CO_{0.2}Fe_{0.8}O_3$ cathode microstructures during sintering: kinetic Monte Carlo (KMC) simulations calibrated by artificial neural networks, J. Power Sources 346 (2017) 103–112, https://doi.org/10.1016/j.jpowsour.2017.02.029.
[51] J.T. Gostick, Versatile and efficient pore network extraction method using marker-based watershed segmentation, Phys. Rev. E. 96 (2017) 023307, https://doi.org/10.1103/PhysRevE.96.023307.
[52] J. Gostick, M. Aghighi, J. Hinebaugh, T. Tranter, M.A. Hoeh, H. Day, B. Spellacy, M.H. Sharqawy, A. Bazylak, A. Burns, W. Lehnert, A. Putz, OpenPNM: a pore network modeling package, Comput. Sci. Eng. 18 (2016) 60–74, https://doi.org/10.1109/mcse.2016.49.
[53] K.M. Graczyk, M. Matyka, Predicting porosity, permeability, and tortuosity of porous media from images by deep learning, Sci. Rep. 10 (2020) 21488, https://doi.org/10.1038/s41598-020-78415-x.
[54] S.J. Cooper, A. Bertei, P.R. Shearing, J.A. Kilner, N.P. Brandon, TauFactor: an open-source application for calculating tortuosity factors from tomographic data, SoftwareX 5 (2016) 203–210, https://doi.org/10.1016/j.softx.2016.09.002.
[55] E.W. Washburn, The dynamics of capillary flow, Phys. Rev. 17 (1921) 273–283, https://doi.org/10.1103/PhysRev.17.273.
[56] Z. Yan, S. Hara, Y. Kim, N. Shikazono, Homogeneity and representativeness analyses of solid oxide fuel cell cathode microstructures, Int. J. Hydrog. Energy 42 (2017) 30166–30178, https://doi.org/10.1016/j.ijhydene.2017.10.096.
[57] Z. Yang, A. Maurey, J. Kang, D.S. Wilkinson, 2D and 3D characterization of pore defects in die cast AM60, Mater. Charact. 114 (2016) 254–262, https://doi.org/10.1016/j.matchar.2016.02.007.
[58] A. Berger, M. Herwegh, J.-O. Schwarz, B. Putlitz, Quantitative analysis of crystal/grain sizes and their distributions in 2D and 3D, J. Struct. Geol. 33 (2011) 1751–1763, https://doi.org/10.1016/j.jsg.2011.07.002.
[59] Y. Hu, A. Patmonoaji, H. Xu, K. Kaito, S. Matsushita, T. Suekane, Pore-scale investigation on nonaqueous phase liquid dissolution and mass transfer in 2D and 3D porous media, Int. J. Heat Mass Transf. 169 (2021) 120901, https://doi.org/10.1016/j.ijheatmasstransfer.2021.120901.
[60] J. Stec, J. Tarasiuk, S. Wroński, R. Filipek, Permeability of micropore carbon materials based on steady-state pore-scale flow calculations in real 2D and 3D microstructures, Ceram. Int. 45 (2019) 17638–17645, https://doi.org/10.1016/j.ceramint.2019.05.329.